Semiconducting Cr$_2$BN monolayer with antiferromagnetic order

Xu Yan [1,*], Fanjunjie Han [2,*], Yansun Yao [3,†], Xiaohua Zhang [1], Yong Liu [1], and Guochun Yang [1,2,‡]

[1]*State Key Laboratory of Metastable Materials Science & Technology and Key Laboratory for Microstructural Material Physics of Hebei Province, School of Science, Yanshan University, Qinhuangdao 066004, China*
[2]*Centre for Advanced Optoelectronic Functional Materials Research and Key Laboratory for UV Light-Emitting Materials and Technology of Northeast Normal University, Changchun 130024, China*
[3]*Department of Physics and Engineering Physics, University of Saskatchewan, Saskatoon, Saskatchewan, Canada S7N 5E2*

The key to the next-generation spintronic devices is to design above-room-temperature two-dimensional antiferromagnets with large magnetic moments and anisotropy energies. We propose a design strategy to maximize the utilization of d electrons and the strong coupling of transition-metal atoms. The designed semiconducting Cr$_2$BN monolayer consists of hexagonal Cr$_6$BN tiles centered by BN dimers. Compared to isolated B or N atoms, the BN dimer in Cr$_2$BN can reduce the charges donated by Cr atoms, whereas the short Cr-Cr distance favors strong direct-exchange coupling interaction. These features make the Cr$_2$BN monolayer checkerboard antiferromagnetic with a high Néel temperature of 874 K, a large magnetic anisotropy energy of 103 μeV/Cr, and a large magnetic moment of 3.79 μ$_B$. High structural stability, originating from the covalent BN dimer and Cr-B/N ionic bond, renders Cr$_2$BN a good candidate for experimental synthesis.

I. INTRODUCTION

Spintronic devices utilize electron spins to achieve information storage, transport, and processing. Made from magnetic materials, these devices have characteristics such as low energy consumption, fast device operation, and high storage density [1,2]. Among various magnetisms [3], antiferromagnetic (AFM) materials have promise for next-generation information technology with robustness against magnetic field perturbation, negligible stray field, ultrafast dynamics, and considerable magnetotransport attribute [4–6]. Some antiferromagnets, such as CuMnAs [7,8] and Mn$_2$Au films [9,10], have achieved electronic write/read functions in memory devices.

Recently discovered intrinsic magnetism in two-dimensional (2D) materials provides new momentum to explore high-speed spintronic nanodevices [11,12]. Progress has been made in finding 2D ferromagnets with higher Curie temperatures [13–15]. Opposite to the well-studied ferromagnetic (FM) materials, more attention should be paid to understanding AFM materials with high Néel temperatures (T_N), closely related to the applications for spintronic devices.

Achieving high transition temperature in magnetic materials requires a larger magnetic moment and strong coupling between magnetic ions [16]. For transition metal (TM) as a magnetic center, the magnitude of the magnetic moment is strongly correlated with the number of unpaired d electrons [3,17]. Thus, minimizing the loss of d electrons (to other orbitals) under specific crystal fields is desirable for producing significant magnetic moments. Also, reducing the distances between them enhances magnetic coupling. Introducing electron-sharing dimers in 2D materials can effectively reduce the electron loss on the TM ions and improve structural stability. Examples include 2D penta−MnN$_2$ with the N$_2$ dimer [18] and 2D TiC$_2$ with the C$_2$ dimer [19].

Bearing this in mind, we use hexagonal TM$_6$ tiles to construct monolayer structures with either X_2 homodimer or XY heterodimer (TM = V, Cr, Mn, Fe, and Co, Ni; X or Y = B, C, N, and P). Similar construction of enclosed covalent dimers in metal hexagons has been predicted in CaSi [20] and transition-metal carbides (TM = Co, Ni, and Cu) [21]. This motif is suggested to have high cohesive energy and kinetic stability. The CoC and NiC monolayers exhibit intrinsic magnetism with a large magnetic anisotropy energy (MAE). The resulting monolayers have TM_2X_2 or TM_2XY composition (Fig. 1), which can bear magnetism of different types. In total, 24 TM_2X_2 and 108 TM_2XY monolayers are considered (Fig. S1 of the Supplemental Material [22], which includes Refs. [23–35]), and four were found dynamically stable, namely, Cr$_2$BN, Co$_2$BN, Mn$_2$BP, and Fe$_2$BN. Interestingly, none of the structures containing X_2 homodimer are dynamically stable. Among the stable structures, Cr$_2$BN shows desirable properties, including a high T_N, a large magnetic anisotropy energy, a large magnetic moment, and a wide band gap. In the following, we focus the discussion on the Cr$_2$BN monolayer.

II. RESULTS AND DISCUSSION

After geometry optimization, the Cr$_2$BN monolayer with imposed periodic boundary condition ($w > 15$ Å vacuum space inserted between layers) is stabilized into an orthorhombic symmetry (space group *Pmma*) (Table S1). The unit cell

---

*These authors contributed equally to this work.
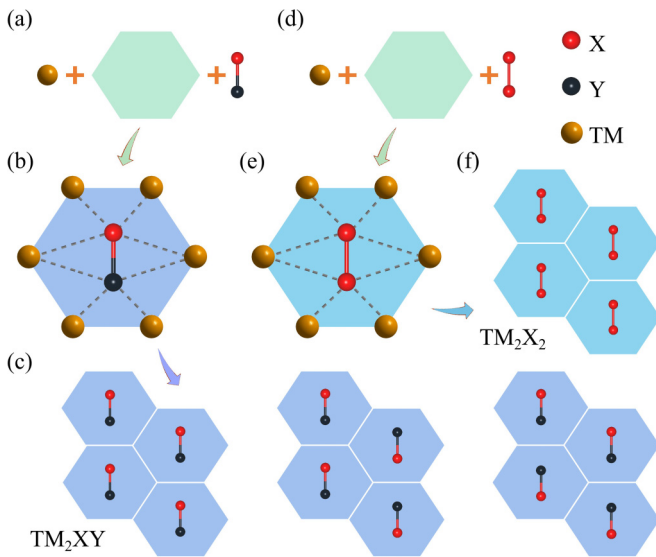†yansun.yao@usask.ca
‡yanggc468@nenu.edu.cn

FIG. 1. (a), (d) Building TM_6XY and TM_6X_2 units. (b), (e) Individual TM_6XY and TM_6X_2 units. (c) Building TM_2XY monolayers using TM_6XY units. Three combined dimer orientations are shown. (f) Assembling TM_2X_2 monolayers using TM_6X_2 units.
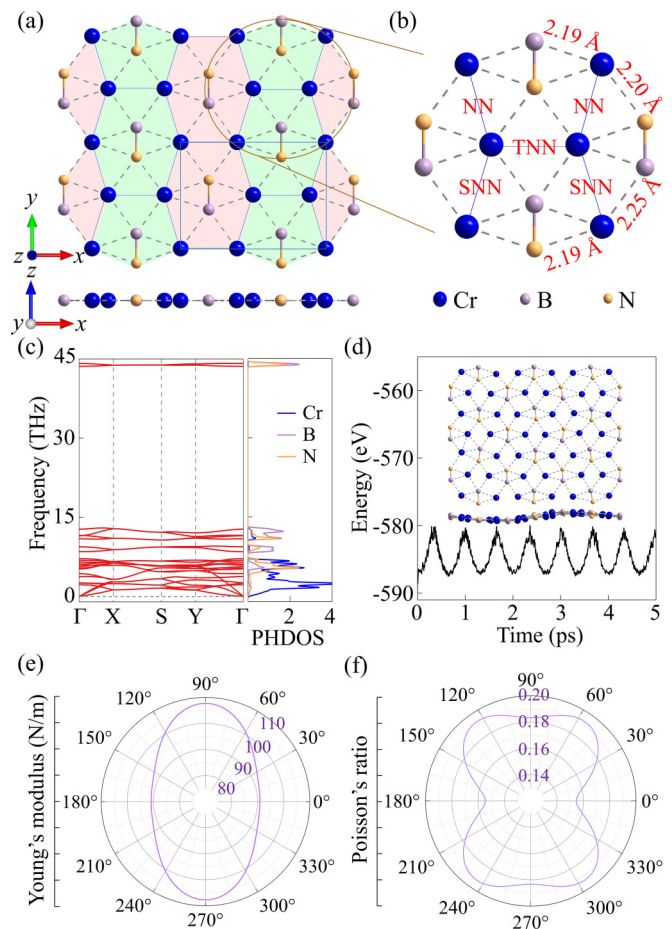

FIG. 2. (a) Top and side views of Cr_2BN monolayer. (b) Enlarged local view. (c) Phonon dispersive curves and density of states of the Cr_2BN. (d) AIMD snapshots (top and side views) of Cr_2BN after 5 ps run at 500 K. (e) Young's modulus and (f) Poisson's ratio of Cr_2BN monolayer.

has 2 formula units [Fig. 2(a)]. In this structure, the BN heterodimers are all parallel or antiparallel, and the hexagonal Cr_6 tiles are stretched along the BN dimers. Each B or N atom is coordinated with four Cr atoms. The BN dimers are aligned along the y-axis to head-to-toe arrays parallel along the x-axis with an alternating half-cell shift [Fig. 2(a)]. The average Cr-B distance (2.22 Å) is slightly larger than the Cr-N distance (2.20 Å). There are three distinct Cr-Cr distances (2.57, 2.63, and 2.64 Å), noted as the nearest (NN), second-nearest (SNN), and third-nearest-neighbors (TNN) in Fig. 2(b). The absence of imaginary frequency in the phonon dispersions confirms the dynamic stability of Cr_2BN [Fig. 2(c)]. The highest frequency is about 44.15 THz, indicating a strong B-N bond. The Cr_2BN maintains its structure (with slight modulation) in *ab initio* molecular dynamics (AIMD) simulations at 500 K [Fig. 2(d)], confirming its thermal stability. The calculated cohesive energy is -4.49 eV per atom, comparable to MoI_3 (-4.35 eV per atom) [36], Fe_2Si (-4.10 eV per atom) [37], and FeB_2 (-4.87 eV per atom) [38] monolayers. The calculated energy of formation (E_f) of Cr_2BN with respect to body-centered-cubic Cr [23], $\alpha-B_{12}$ [24], and α-N [25] is -0.58 eV per atom. The negative E_f suggests the possibility of synthesizing the Cr_2BN monolayer in the lab.

Suitable substrate material is crucial to the monolayer synthesis. The Cr_2BN monolayer with a 3×1 supercell matches well with the Al (111) $7 \times \sqrt{3}$ supercell (i.e., a 3% lattice mismatch). Based on the difference charge density (Fig. S2) and the binding energy of 69 meV/Å^2, the Cr_2BN monolayer might be stabilized and exfoliated on Al (111) substrate [39,40]. The calculated elastic constants ($C_{11} = 93.49$ N/m, $C_{12} = 17.14$ N/m, $C_{22} = 110.86$ N/m, and $C_{66} = 40.31$ N/m) satisfy the Born stability criterion ($C_{11}, C_{66} > 0$ and $C_{11}C_{22} > C_{12}^2$). Young's modulus and Poisson's ratio show obvious anisotropic characters [Figs. 2(e) and 2(f)]. Young's modulus of Cr_2BN ranges from $90.8 \sim 107.7$ N/m, comparable to

synthetic $2H-MoS_2$ (130 N/m) [41] and NbS_2 (96 N/m) [42] monolayers, and its Poisson's ratio of $0.15 \sim 0.19$ is almost equal to 0.19 in graphene [43].

By comparing the energies of different magnetic configurations, the magnetic ground state of the Cr_2BN monolayer is found to be the checkerboard antiferromagnetic [Fig. 3(a)], with the energy difference of 1.05, 0.88, 0.63, and 0.47 eV/f.u. in comparison with the four other magnetic states, respectively. The spin-charge density [Fig. 3(b)] confirms that the magnetism is entirely due to Cr ions with a magnetic moment of 3.79 μ_B, corresponding to nominal Cr^{2+}. The four valence electrons on Cr^{2+} occupy four nondegenerate 3d orbitals, leading to a high spin state [Fig. 4(c)]. This can be attributed to the large splitting between spin-up and spin-down channels [Fig. 4(b)]. Each BN dimer [Fig. 4(e)] accepts four electrons [Fig. 4(d)] to form a double bond. The B = N distance of 1.39 Å in the Cr_2BN is comparable to the B = N bond length in H_2BNH_2 (1.39 Å) and $Cl_2BN(H)C_6H_5$ (1.38 Å) [44]. Compared with isolated B/N atoms, the covalent BN dimers in the Cr_2BN monolayer have fewer empty p orbitals, which accept less d electrons. This results in a higher magnetic moment in Cr_2BN than in CrB (3.50 μ_B) [45] and CrN (3.00 μ_B) [46] monolayers.
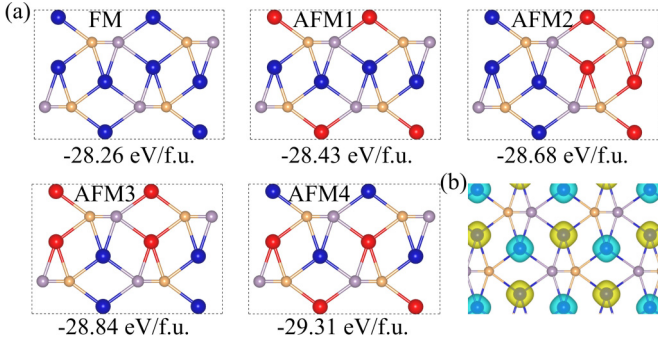
FIG. 3. (a) Five magnetic configurations of Cr$_2$BN monolayer; red and blue spheres represent spin-up and spin-down Cr atoms, respectively. (b) Spin-charge density of Cr$_2$BN monolayer, in which blue and yellow represent different spin states, respectively.

FIG. 5. Schematic diagrams of (a) direct-exchange and (b) two superexchange paths mediated by B/N atom. (c) Schematic diagrams of magnetic exchange interaction and corresponding coupling strength of NN, SNN, and TNN Cr pairs, "$\oplus$" represents synergistic effect between exchange coupling interactions.

As shown in Fig. 4(a), Cr$_2$BN is a semiconductor with an indirect band gap of 2.31 eV at the revised Heyd-Scuseria-Ernzerhof screened hybrid functional (HSE06) level, much larger than the typical semiconducting MoS$_2$ (1.85 eV) [47]. A wide band gap favors applications in high-energy electronic devices [48]. The conduction-band minimum is mainly contributed by Cr-d_{yz}, B-p_z, and N-p_z states, while the valence-band maximum by the hybridization between Cr-d_{xy}, B-p_x, and N-p_x states [Fig. 4(b)]. There appears to be strong orbital hybridization in the BN pair.

Antiferromagnetism in Cr$_2$BN monolayer is originated from the competition between direct- and superexchange interactions. Direct-exchange interaction is based on the overlap of wave functions, which in many cases prefers antiferromag-
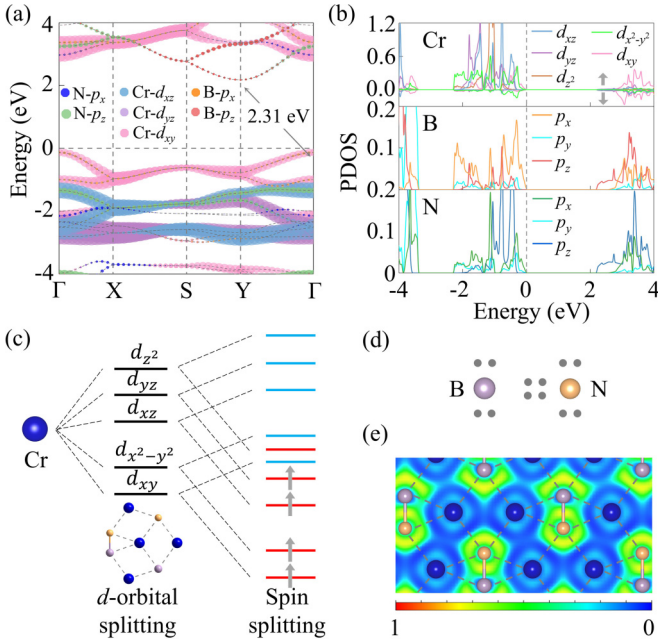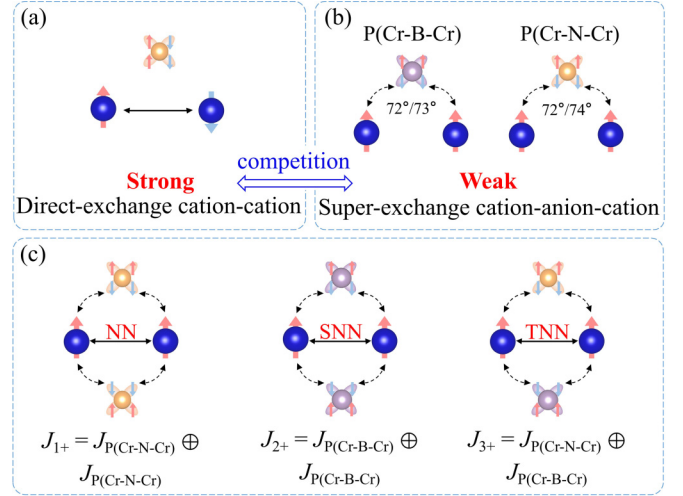

FIG. 4. (a) Electronic band structure and (b) projected density of states (PDOS) of Cr$_2$BN calculated at HSE06 level. (c) Schematic diagram of orbitals splitting and occupations for Cr-d orbitals in Cr$_2$BN monolayer. (d) Configuration of BN. (e) Electron localization function map.

netic configuration with paired spins (energetically favorable). Bulk Cr is the only elemental solid that shows antiferromagnetic ordering at ambient conditions. Cr$_2$BN monolayers have Cr-Cr distances close to that in bulk Cr (2.49 Å) [35], which induce strong direct-exchange interaction for AFM coupling [Fig. 5(a)]. The two superexchange paths are mediated by B and N atoms, respectively [P(Cr-B-Cr) and P(Cr-N-Cr) in Fig. 5(b)] with path angles of $72° \sim 74°$. According to the Goodenough-Kanamori-Anderson rules [49,50], these two paths favor FM coupling. Since the path angles deviate from the ideal right angle [Fig. 5(b)] [51,52], they result in weaker interactions. Geometrically, the strengths of ferromagnetic couplings for three Cr pairs (J_{1+}, J_{2+}, and J_{3+}) are determined by superexchange interactions along two P(Cr-N-Cr) paths, two P(Cr-B-Cr) paths, and one P(Cr-N-Cr) path and one P(Cr-B-Cr) path, respectively [Fig. 5(c)]. The absence of spin polarization on B/N atoms limits the electron hopping in the superexchange channel [53,54], weakening the strength of the superexchange interaction. Overall, direct-exchange coupling interaction plays a dominant role in the AFM Cr$_2$BN monolayer.

The magnetic exchange coupling strength and T_N are calculated with a classic Heisenberg spin Hamiltonian,

$$\hat{H} = E_0 - \sum_{ij} J_1 \vec{S_i} \vec{S_j} - \sum_{ik} J_2 \vec{S_i} \vec{S_k} - \sum_{ih} J_3 \vec{S_i} \vec{S_h} + A \sum_l S_l^{z2},$$

$$(1)$$

where E_0 represents the energy of the paramagnetic state. J_1, J_2, and J_3 are the magnetic exchange coupling parameters between NN, SNN, and TNN Cr atoms. A denotes the single-ion anisotropy parameter. The value of A is calculated to be -0.01 meV. S represents the spin quantum number of magnetic Cr ions, taken as 2 here. The resulting values of J_1, J_2, and J_3 are -21.16, -92.77, and -62.52 meV, exchange coupling matrices of which can be found in Table S2. These values are comparable with the ones in other Cr-based AFM
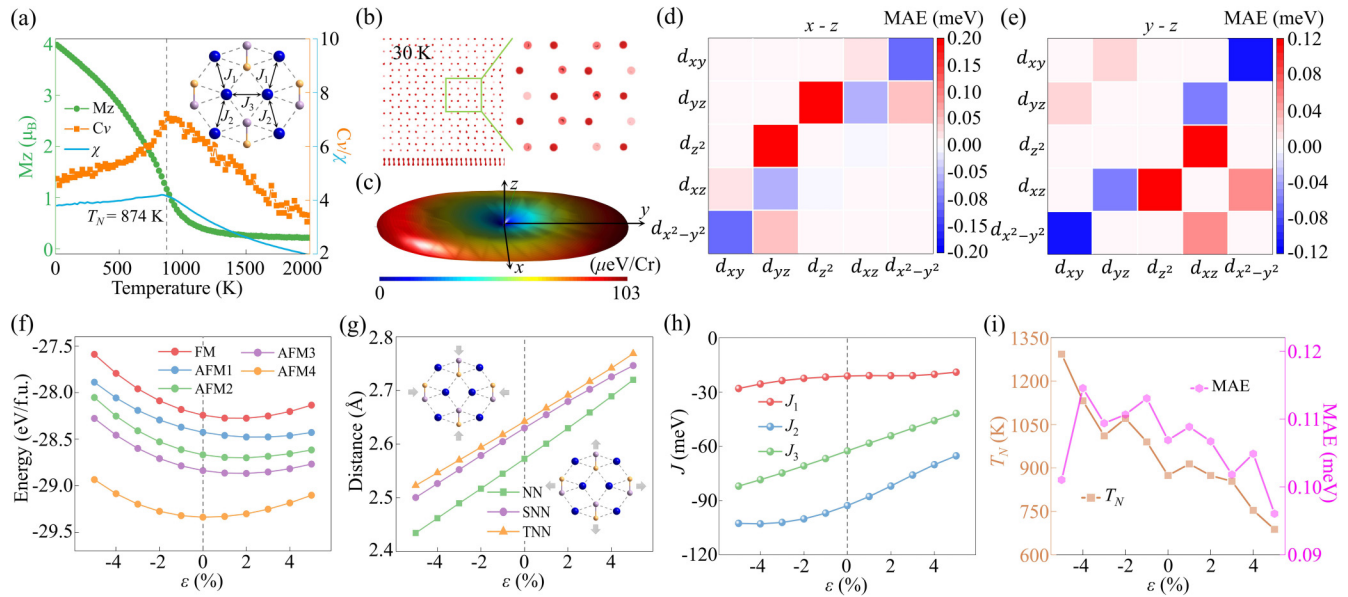
FIG. 6. (a) Temperature-dependent variation of average magnetic moment of Cr ion (green), specific heat (yellow), and susceptibility (blue) of Cr_2BN monolayer derived from Monte Carlo simulations based on classical Heisenberg model. (b) Top and side views of real-space alignment of magnetic moments after Monte Carlo simulations at $T = 30$ K (left) and enlarged local view (right), in which red and pink in top view represent totally spin-up and spin-down magnetization, respectively. (c) Three-dimensional MAE of Cr_2BN monolayer. In plane along x direction (d) and y direction (e) vs out-of-plane difference $\Delta E_{SOC} = E_{SOC,x/y} - E_{SOC,z}$ for Cr $3d$ orbitals. (f) Energies of five magnetic configurations of Cr_2BN monolayer under biaxial strain. (g) Distances between NN, SNN, and TNN Cr atoms under biaxial strain. (h) Response of J_1, J_2, and J_3 under biaxial strain. (i) T_N and MAE under different biaxial strains.

monolayers, such as $CrBO_3$ (-80.49 meV) [28] and Cr_2CXX' (X, X' = H, F, Cl, Br, OH) ($-16.35 \sim -24.58$ meV) [55]. The AFM coupling strength in Cr pairs is related to the Cr-Cr distance and the surroundings.

The Monte Carlo (MC) simulations show that the T_N is up to 874 K [Fig. 6(a)], which is much higher than the reported 2D AFM semiconductors, such as Mn_2C (720 K) [56], $CrBO_3$ (397 K) [28], and Cr_2CXX' (X, X' = H, F, Cl, Br, OH) ($270 \sim 430$ K) monolayers [55]. The representative real-space alignment of magnetic moments after the MC simulations is shown in Figs. 6(b) and S3. The out-of-plane checkerboard AFM ordering is observed under 30 K, which agrees with the ground magnetic ordering of density-functional theory calculations [Fig. 6(b)]. With the increase in temperature, the alignment of magnetic moments gradually becomes disordered (Fig. S3). These results indicate that the Cr_2BN monolayer has the ability to overcome the spin flipping caused by room-temperature thermal perturbation, facilitating the application in spintronic devices.

A large magnetic anisotropy energy (MAE) is advantageous for enhancing the stability of long-range magnetic ordering in 2D materials. The angular-dependence MAE of the Cr_2BN monolayer is calculated by rotating spins in the $xy/yz/xz$ planes. The resulting magnetic easy axis is along the out-of-plane direction [Fig. 6(c)], consistent with the alignment of magnetic moments of MC simulation. Herein, the magnetic anisotropy of the Cr_2BN monolayer comes from exchange anisotropy and single-ion anisotropy. The calculated MAE is 103 µeV/Cr, larger than $CrSnTe_3$ (69 µeV/Cr) [57], $CrCl_3$ (25 µeV/Cr) [58], and Fe monolayer/Rh (111) (80 µeV/Fe) [59]. Furthermore, the contribution of the spin-orbital coupling (SOC) interaction between the Cr-d orbitals

to the magnetic anisotropy can be reflected by the orbital-resolved MAE [60] [Figs. 6(d) and 6(e)]. Negative MAE is mainly contributed by the coupling of (d_{xy}, $d_{x^2-y^2}$). The hybridization between ($d_{xz/yz}$, d_{z^2}), ($d_{xz/yz}$, $d_{x^2-y^2}$), and ($d_{xz/yz}$, d_{xy}) leads to positive MAE in the Cr_2BN monolayer, corresponding to the out-of-plane easy axis.

The key magnetic parameters of the Cr_2BN monolayer under biaxial and uniaxial strains along the x and y directions are characterized. The AFM ground state is maintained [Fig. 6(f)] under -5 to 5% strain. The band gap gradually increases from 1.13 to 1.63 eV from biaxial compressive to tensile strain based on generalized gradient approximation (GGA)+U level (the Coulomb interaction parameter U value is assumed to be 3.0 eV). This level of theory is commonly used for describing the band-gap change (Fig. S4). From biaxial compressive to tensile strain, the distances of neighboring Cr ions are gradually elongated [Fig. 6(g)]. Besides, as the distance between the neighboring Cr atoms increases with the external strain from -5 to 5%, the direct-exchange interactions are weakened, leading to reduced J_1, J_2, and J_3 [Fig. 6(h)]. Nevertheless, the T_N remains well above room temperature in the considered strain range [Fig. 6(i)]. On the other hand, the magnetic easy axis still points out of plane, and the MAE ($108 \sim 115$ µeV) is enhanced under suitable strain regulation ($-4 \sim 1$%) and reaches the maximum (115 µeV) under -4% compressive strain [Fig. 6(i)]. Under the uniaxial strain, Js and T_N also have similar trends to the biaxial strain (Figs. S5 and S6).

III. CONCLUSIONS

Considering that the covalent main-group element dimer enhances structural stability and shorter interatomic

distance favors direct-exchange coupling interaction, we used the designed hexagonal TM_6XY unit to build the TM_2X_2 ($X = Y$) and TM_2XY ($X \neq Y$) monolayers. Four stable magnetic monolayers (e.g., Cr$_2$BN, Co$_2$BN, Mn$_2$BP, and Fe$_2$BN) are unveiled, among which the Cr$_2$BN monolayer shows desirable AFM semiconductor characteristics. This includes a high T_N of 874 K, a large perpendicular MAE of 103 μeV/Cr, a magnetic moment of 3.79 μ$_B$, and a wide band gap of 2.31 eV. Moreover, the semiconducting and high-temperature AFM properties can be maintained under biaxial strain from $-5 \sim 5\%$. Our study introduces an idea to design high-performance magnetic materials.

[1] S. A. Wolf, D. D. Awschalom, A. Buhrman, M. Daughton, S. von Molnár, M. L. Roukes, A. Y. Chtchelkanova, and D. M. Treger, Spintronics: A spin-based electronics vision for the future, Science **294**, 1488 (2021).

[2] A. Chen, Y. Wen, B. Fang, Y. Zhao, Q. Zhang, Y. Chang, P. Li, H. Wu, H. Huang, Y. Lu *et al.*, Giant nonvolatile manipulation of magnetoresistance in magnetic tunnel junctions by electric fields via magnetoelectric coupling, Nat. Commun. **10**, 243 (2019).

[3] X. Jiang, Q. Liu, J. Xing, N. Liu, Y. Guo, Z. Liu, and J. Zhao, Recent progress on 2D magnets: Fundamental mechanism, structural design and modification, Appl. Phys. Rev. **8**, 031305 (2021).

[4] X. Marti, I. Fina, C. Frontera, J. Liu, P. Wadley, Q. He, R. J. Paull, J. D. Clarkson, J. Kudrnovsky, I. Turek *et al.*, Room-temperature antiferromagnetic memory resistor, Nat. Mater. **13**, 367 (2014).

[5] T. Jungwirth, X. Marti, P. Wadley, and J. Wunderlich, Antiferromagnetic spintronics, Nat. Nanotechnol. **11**, 231 (2016).

[6] V. Baltz, A. Manchon, M. Tsoi, T. Moriyama, T. Ono, and Y. Tserkovnyak, Antiferromagnetic spintronics, Rev. Mod. Phys. **90**, 015005 (2018).

[7] P. Wadley, B. Howells, J. Železný, C. Andrews, V. Hills, R. P. Campion, V. Novák, K. Olejník, F. Maccherozzi, S. S. Dhesi *et al.*, Electrical switching of an antiferromagnet, Science **351**, 587 (2016).

[8] K. Olejník, V. Schuler, X. Marti, V. Novák, Z. Kašpar, P. Wadley, R. P. Campion, K. W. Edmonds, B. L. Gallagher, J. Garces *et al.*, Antiferromagnetic CuMnAs multi-level memory cell with microelectronic compatibility, Nat. Commun. **8**, 15434 (2017).

[9] S. Y. Bodnar, L. Šmejkal, I. Turek, T. Jungwirth, O. Gomonay, J. Sinova, A. A. Sapozhnik, H. J. Elmers, M. Kläui, and M. Jourdan, Writing and reading antiferromagnetic Mn$_2$Au by Néel spin-orbit torques and large anisotropic magnetoresistance, Nat. Commun. **9**, 348 (2018).

[10] M. Meinert, D. Graulich, and T. Matalla-Wagner, Electrical switching of antiferromagnetic Mn$_2$Au and the role of thermal activation, Phys. Rev. Appl. **9**, 064040 (2018).

[11] E. C. Ahn, 2D materials for spintronic devices, NPJ 2D Mater. Appl. **4**, 17 (2020).

[12] M. Hossain, B. Qin, B. Li, and X. Duan, Synthesis, characterization, properties and applications of two-dimensional magnetic materials, Nano Today **42**, 101338 (2022).

[13] M. Bonilla, S. Kolekar, Y. Ma, H. C. Diaz, V. Kalappattil, R. Das, T. Eggers, H. R. Gutierrez, M. H. Phan, and M. Batzill, Strong room-temperature ferromagnetism in VSe$_2$ monolayers on van der Waals substrates, Nat. Nanotechnol. **13**, 289 (2018).

[14] J. Li, B. Zhao, P. Chen, R. Wu, B. Li, Q. Xia, G. Guo, J. Luo, K. Zang, Z. Zhang *et al.*, Synthesis of ultrathin metallic MTe$_2$ (M = V, Nb, Ta) single-crystalline nanoplates, Adv. Mater. **30**, 1801043 (2018).

[15] D. J. O'Hara, T. Zhu, A. H. Trout, A. S. Ahmed, Y. K. Luo, C. H. Lee, M. R. Brenner, S. Rajan, J. A. Gupta, D. W. McComb *et al.*, Room temperature intrinsic ferromagnetism in epitaxial manganese selenide films in the monolayer limit, Nano Lett. **18**, 3125 (2018).

[16] Z.-X. Shen, C. Su, and L. He, High-throughput computation and structure prototype analysis for two-dimensional ferromagnetic materials, npj Comput. Mater. **8**, 132 (2022).

[17] C. M. Acosta, E. Ogoshi, J. A. Souza, and G. M. Dalpian, Machine learning study of the magnetic ordering in 2D materials, ACS Appl. Mater. Interfaces **14**, 9418 (2022).

[18] K. Zhao and Q. Wang, High Curie temperature ferromagnetism in penta$-$MnN$_2$ monolayer, Appl. Surf. Sci. **505**, 144620 (2020).

[19] T. Zhao, S. Zhang, Y. Guo, and Q. Wang, TiC$_2$: A new two-dimensional sheet beyond MXenes, Nanoscale **8**, 233 (2016).

[20] Y. Wang, M. Qiao, Y. Li, and Z. Chen, A two-dimensional CaSi monolayer with quasi-planar pentacoordinate silicon, Nanoscale Horiz. **3**, 327 (2018).

[21] C. Zhu, H. Lv, X. Qu, M. Zhang, J. Wang, S. Wen, Q. Li, Y. Geng, Z. Su, X. Wu *et al.*, TMC (TM = Co, Ni, and Cu) monolayers with planar pentacoordinate carbon and their potential applications, J. Mater. Chem. C **7**, 6406 (2019).

[22] See Supplemental Material at http://link.aps.org/supplemental/10.1103/PhysRevB.108.174402 for computational details, structural, electronic, and magnetic properties, and supplemental tables (includes Refs. [23–35]).

[23] A. W. Hull, X-ray crystal analysis of thirteen common metals, Phys. Rev. **17**, 571 (1921).

[24] L. V. McCarty, J. S. Kasper, F. H. Horn, B. F. Decker, and A. E.Newkirk., A new crystalline modification of boron, J. Am. Chem. Soc. **80**, 2592 (1958).

[25] J. Donohue, A refinement of the positional parameter in a-nitrogen, Acta Crystallogr. **14**, 1000 (1961).

[26] G. Kresse and J. Furthmüller, Efficient iterative schemes for ab initio total-energy calculations using a plane-wave basis set, Phys. Rev. B **54**, 11169 (1996).

[27] J. P. Perdew, K. Burke, and M. Ernzerhof, Generalized gradient approximation made simple, Phys. Rev. Lett. **77**, 3865 (1996).

[28] D. Wu, Z. Zhuo, H. Lv, K. Zhang, Y. Ji, P. Wang, X. Luo, X. Wu, and J. Yang, First-principles calculations of room-temperature antiferromagnetism in crystalline transition-metal borate nanosheets: Implications for spintronics applications, ACS Appl. Nano Mater. **4**, 10877 (2021).

[29] Q. Wu, Y. Zhang, Q. Zhou, J. Wang, and X. C. Zeng, Transition-metal dihydride monolayers: A new family of two-dimensional ferromagnetic materials with intrinsic room-temperature half-metallicity, J. Phys. Chem. Lett. **9**, 4260 (2018).

[30] L. Zhou, F. Körmann, D. Holec, M. Bartosik, B. Grabowski, J. Neugebauer, and P. H. Mayrhofer, Structural stability and thermodynamics of CrN magnetic phases from ab initiocalculations and experiment, Phys. Rev. B **90**, 184102 (2014).

[31] P. E. Blöchl, Projector augmented-wave method, Phys. Rev. B **50**, 17953 (1994).

[32] A. Togo, F. Oba, and I. Tanaka, First-principles calculations of the ferroelastic transition between rutile-type and $CaCl_2$−type SiO_2 at high pressures, Phys. Rev. B **78**, 134106 (2008).

[33] G. Martyna, M. Klein, and M. Tuckerman, Nosé-Hoover chains: The canonical ensemble via continuous dynamics, J. Chem. Phys. **97**, 2635 (1992).

[34] J. Heyd, G. E. Scuseria, and M. Ernzerhof, Hybrid functionals based on a screened Coulomb potential, J. Chem. Phys. **118**, 8207 (2003).

[35] L. Liu, X. Ren, J. Xie, B. Cheng, W. Liu, T. An, H. Qin, and J. Hu, Magnetic switches via electric field in BN nanoribbons, Appl. Surf. Sci. **480**, 300 (2019).

[36] J. Zhang, B. Zhao, C. Ma, and Z. Yang, Bipolar ferromagnetic semiconductors and doping-tuned room-temperature half-metallicity in monolayer MoX_3 (X = Cl, Br, I) : An HSE06 study, Phys. Rev. B **103**, 075433 (2021).

[37] Y. Sun, Z. Zhuo, X. Wu, and J. Yang, Room-temperature ferromagnetism in two-dimensional Fe_2Si nanosheet with enhanced spin-polarization ratio, Nano Lett. **17**, 2771 (2017).

[38] H. Zhang, Y. Li, J. Hou, A. Du, and Z. Chen, Dirac state in the FeB_2 monolayer with graphene-like boron sheet, Nano Lett. **16**, 6124 (2016).

[39] N. Mounet, M. Gibertini, P. Schwaller, D. Campi, A. Merkys, A. Marrazzo, T. Sohier, I. E. Castelli, A. Cepellotti, G. Pizzi *et al.*, Two-dimensional materials from high-throughput computational exfoliation of experimentally known compounds, Nat. Nanotechnol. **13**, 246 (2018).

[40] X. Zhou, Y. Hang, L. Liu, Z. Zhang, and W. Guo, A large family of synthetic two-dimensional metal hydrides, J. Am. Chem. Soc. **141**, 7899 (2019).

[41] R. C. Cooper, C. Lee, C. A. Marianetti, X. Wei, J. Hone, and J. W. Kysar, Nonlinear elastic behavior of two-dimensional molybdenum disulfide, Phys. Rev. B **87**, 035423 (2013).

[42] Y. Zang, Y. Ma, R. Peng, H. Wang, B. Huang, and Y. Dai, Large valley-polarized state in single-layer NbX_2 (X = S, Se): Theoretical prediction, Nano Res. **14**, 834 (2020).

[43] A. Politano, A. R. Marino, D. Campi, D. Farías, R. Miranda, and G. Chiarello, Elastic properties of a macroscopic graphene sample from phonon dispersion measurements, Carbon **50**, 4903 (2012).

[44] S. Berski, Z. Latajka, and A. J. Gordon, On the multiple B-N bonding in boron compounds using the topological analysis of electron localization function (ELF), New J. Chem. **35**, 89 (2011).

[45] M. Dou, H. Li, Q. Yao, J. Wang, Y. Liu, and F. Wu, Room-temperature ferromagnetism in two-dimensional transition metal borides: A first-principles investigation, Phys. Chem. Chem. Phys. **23**, 10615 (2021).

[46] A. V. Kuklin, A. A. Kuzubov, E. A. Kovaleva, N. S. Mikhaleva, F. N. Tomilin, H. Lee, and P. V. Avramov, Two-dimensional hexagonal CrN with promising magnetic and optical properties: A theoretical prediction, Nanoscale **9**, 621 (2017).

[47] A. Splendiani, L. Sun, Y. Zhang, T. Li, J. Kim, C. Y. Chim, G. Galli, and F. Wang, Emerging photoluminescence in monolayer MoS_2, Nano Lett. **10**, 1271 (2010).

[48] G. Schusteritsch, M. Uhrin, and C. J. Pickard, Single-layered Hittorf's phosphorus: A wide-bandgap high mobility 2D naterial, Nano Lett. **16**, 2975 (2016).

[49] J. B. Goodenough, Theory of the role of covalence in the perovskite-type manganites [La, M(II)]MnO_3, Phys. Rev. **100**, 564 (1955).

[50] J. B. Goodenough, An interpretation of the magnetic properties of the perovskite-type mixed crystals $La_{1−x}Sr_xCoO_3$, J. Phys. Chem. Solids **6**, 287 (1958).

[51] S. V. Streltsov and D. I. Khomskii, Electronic structure and magnetic properties of pyroxenes (Li, Na)TM(Si, Ge)$_2O_6$: Low-dimensional magnets with 90° bonds, Phys. Rev. B **77**, 064405 (2008).

[52] B. Wang, X. Zhang, Y. Zhang, S. Yuan, Y. Guo, S. Dong, and J. Wang, Prediction of a two-dimensional high−T_C f-electron ferromagnetic semiconductor, Mater. Horiz. **7**, 1623 (2020).

[53] G. Song, D. Li, H. Zhou, C. Zhang, Z. Li, G. Li, B. Zhang, X. Huang, and B. Gao, Intrinsic room-temperature ferromagnetic semiconductor $InCrTe_3$ monolayers with large magnetic anisotropy and large piezoelectricity, Appl. Phys. Lett. **118**, 123102 (2021).

[54] J. Xiao, D. Legut, W. Luo, H. Guo, X. Liu, R. Zhang, and Q. Zhang, Modulating superexchange strength to achieve robust ferromagnetic couplings in two-dimensional semiconductors, Phys. Rev. B **101**, 014431 (2020).

[55] J. He, P. Lyu, L. Z. Sun, Á. Morales García, and P. Nachtigall, High temperature spin-polarized semiconductivity with zero magnetization in two-dimensional Janus MXenes, J. Mater. Chem. C **4**, 6500 (2016).

[56] L. Hu, X. Wu, and J. Yang, Mn_2C monolayer: A 2D antiferromagnetic metal with high Néel temperature and large spin-orbit coupling, Nanoscale **8**, 12939 (2016).

[57] H. L. Zhuang, Y. Xie, P. R. C. Kent, and P. Ganesh, Computational discovery of ferromagnetic semiconducting single-layer $CrSnTe_3$, Phys. Rev. B **92**, 035407 (2015).

[58] L. Webster and J.-A. Yan, Strain-tunable magnetic anisotropy in monolayer $CrCl_3$, $CrBr_3$, and CrI_3, Phys. Rev. B **98**, 144411 (2018).

[59] A. Lehnert, S. Dennler, P. Błoński, S. Rusponi, M. Etzkorn, G. Moulas, P. Bencok, P. Gambardella, H. Brune, and J. Hafner, Magnetic anisotropy of Fe and Co ultrathin films deposited on Rh(111) and Pt(111) substrates: An experimental and first-principles investigation, Phys. Rev. B **82**, 094409 (2010).

[60] A. Halder, S. Bhandary, D. D. O'Regan, S. Sanvito, and A. Droghetti, Theoretical perspective on the modification of the magnetocrystalline anisotropy at molecule-cobalt interfaces, Phys. Rev. Mater. **7**, 064409 (2023).